Acta Crystallographica Section B
Structural Science
ISSN 0108-7681

Weak intra- and intermolecular interactions in a binaphthol imine: an experimental charge-density study on (±)-8′-benzhydrylideneamino-1,1′-binaphthyl-2-ol

Louis J. Farrugia,* Pavel Kočovský, Hans Martin Senn and Štěpán Vyskočil

WestCHEM, Department of Chemistry, University of Glasgow, Glasgow G12 8QQ, Scotland

Correspondence e-mail: louis@chem.gla.ac.uk

Received 28 May 2009
Accepted 17 August 2009

The charge density in (±)-8′-benzhydrylideneamino-1,1′-binaphthyl-2-ol (1) has been studied experimentally using Mo $K\alpha$ X-ray diffraction at 100 K, and by theory using density-functional thoery (DFT) calculations at the B3LYP/6-311++G** level. The nature of the weak intramolecular *peri*-C···N, CH···π, H···H and C(π)···C(π) interactions has been examined by topological analysis using the Quantum Theory of Atoms in Molecules (QTAIM) approach. An analysis of the density $\rho(\mathbf{r})$, the Laplacian of the density $\nabla^2\rho(\mathbf{r}_b)$ and other topological properties at the bond-critical points were used to classify these interactions. The study confirms the presence of the intramolecular CH···π interaction in (1), which was previously suspected on geometrical grounds. An analysis of the ellipticity profiles along the bond paths unambiguously shows the π-delocalization between the imine unit and one *N*-phenyl group. The weak intermolecular interactions in the crystal of (1) were examined experimentally and theoretically through the pairwise interactions of the seven independent dimeric pairs of (1) responsible for the set of unique intermolecular interactions, and also through examination of the Hirshfeld surface d_{norm} property. The theoretical dimeric-pair calculations used the BLYP-D functional which supplements the exchange-correlational functional with an empirical dispersion term to provide a more accurate determination of the energies for the weak intermolecular interactions.

1. Introduction

In the last two decades with the advances in topological charge-density methods (Koritsanszky & Coppens, 2001) there has been intensive interest in the study of weak intra- and intermolecular interactions, especially hydrogen bonds, using these methods (Espinosa *et al.*, 1999; Gatti *et al.*, 2002; Munshi & Guru Row, 2005*a*,*b*,*c*). Interest in the fundamental nature of these bonds has been stimulated by the very topical areas of supramolecular chemistry and crystal engineering (Desiraju, 1989). Weak hydrogen bonds involving CH···*X* interactions (Steiner, 1996; Desiraju & Steiner, 2001) have been particularly investigated, as they have been quite controversial in the past, although they are now generally accepted as genuine hydrogen bonds (see Jeffrey, 1999, for a recent overview).

The AIM (Atoms in Molecules) theory of Bader (1990) has been central to the understanding of weak interactions, and early studies by Cioslowski *et al.* (1991) and Cioslowski & Mixon (1992) have pointed out the utility of this approach. Koch & Popelier (1995) have proposed a set of AIM criteria to distinguish CH···O bonds from van der Waals interactions on the basis of their charge density. These are now extensively utilized, see for example Gatti *et al.* (2002). In a number of

Table 1
Experimental details.

Crystal data	
Chemical formula	$C_{33}H_{23}NO$
M_r	449.52
Crystal system, space group	Monoclinic, $P2_1/c$
Temperature (K)	100
a, b, c (Å)	11.1055 (1), 11.6712 (1), 18.0627 (1)
β (°)	102.6753 (3)
V (Å^3)	2284.13 (3)
Z	4
$F(000)$	944
D_x (g cm^{-3})	1.307
Radiation type	Mo $K\alpha$
λ (Å)	0.71073
θ range (°) for cell measurement	2.9–41.2
μ (mm^{-1})	0.08
Colour	Pale straw yellow
Crystal size (mm)	0.53 × 0.5 × 0.37
Data collection	
Diffractometer	KappaCCD
Absorption correction	Multi-scan (Blessing, 1995)
T_{max}, T_{min}	0.954, 1.01
$\sin(\theta_{max})/\lambda$	1.079
No. of measured, independent and observed $[I > 2\sigma(I)]$ reflections	358 895, 23 246, 19 025
R_{int}	0.036
R_σ	0.018
Spherical atom refinement	
No. of data in refinement	23 246
No. of refined parameters	317
Final R $[I > 2\sigma(I)]$ (all data), wR^2 $[I > 2\sigma(I)]$ (all data)	0.0423 (0.0549), 0.1254 (0.1325)
Goodness-of-fit S	1.014
Largest features in residual density map (e Å^{-3})	0.675, −0.243
Max shift/e.s.d. in last cycle	$< 10^{-3}$
Multipole refinement	
No. of data in refinement	19 692
No. of refined parameters	1066
Final R $[F > 2\sigma(F)]$ (all data), wR^2 $[F > 2\sigma(F)]$	0.0239 (0.0423), 0.0291
Goodness-of-fit S	1.768
Largest features in residual density map, all data ($\sin\theta/\lambda \leq 0.8$ Å^{-1}) (e Å^{-3})	0.246, −0.199 (0.098, −0.074)
Max shift/e.s.d. in last cycle	5.8×10^{-6}

$R = \Sigma(|F_o| - |F_c|)/\Sigma(F_o)$, $R_2 = \Sigma(F_o^2 - F_c^2)/\Sigma(F_o^2)$; $wR^2 = \Sigma(w(F_o^2 - F_c^2)^2)/\Sigma(w(F_o^2)^2)^{1/2}$, $R_\sigma = \Sigma[\sigma(F_o^2)]/\Sigma[F_o^2]$; $R_{int} = \Sigma n/(n - 11/2|F_o^2 - F_o^2(\text{mean})|/\Sigma F_o^2$ (summation is carried out only where more than one symmetry equivalent is averaged). Computer programs used: *COLLECT* (Nonius, 1998), *HKL SCALEPACK* and *DENZO* (Otwinowski & Minor, 1997), *SHELXS*97 and *SHELXL*97 (Sheldrick, 2008), *ORTEP*3 for Windows (Farrugia, 1997), *WinGX* publication routines (Farrugia, 1999).

studies, Espinosa and co-workers (see Mata *et al.*, 2007, for a recent summary) have proposed linear, exponential or Morse-like relationships between hydrogen-bonding geometrical parameters, such as $d(H\cdots O)$ and charge-density indicators, such as the density at the bond-critical point (b.c.p.), $\rho(\mathbf{r}_b)$, the Laplacian of the charge density at the b.c.p., $\nabla^2\rho(\mathbf{r}_b)$, the local kinetic and potential energy densities, $G(\mathbf{r}_b)$ and $V(\mathbf{r}_b)$, and the $\lambda_3(\mathbf{r}_b)$ Hessian eigenvalue. Mallinson *et al.* (2003) and Munshi & Guru Row (2005*a*,*b*) have proposed similar relationships, which may hold over a wide range of chemical interactions, including quite strong covalent bonds.

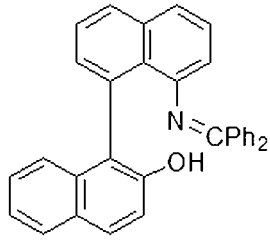

(±)-**1**

The X-ray crystal structure of racemic hydroxy imine (1), a synthetic intermediate in the preparation of chiral auxiliaries, has been previously reported (Vyskočil *et al.*, 2002). The structure showed evidence for a $CH\cdots\pi$ interaction between an *ortho* CH group on one of the phenyl rings and one of the benzene rings of the naphthyl group bearing the OH substituent. Another point of interest is the nature of the through-space *peri* interaction in 1,8-disubstituted naphthalene rings. Since (1) forms excellent quality crystals, a full experimental charge-density study was undertaken to examine these and other weak interactions in more detail using the AIM methodology.

2. Experimental procedures

2.1. Data collection, processing and spherical atom refinement

Compound (1) was recrystallized from acetonitrile. The specimen investigated was cleaved from a larger crystal to give an approximately isotropic sample. Details of data collection and refinement procedures are given in Table 1. The crystal was cooled from ambient temperature to 100 K over a period of 1 h, using an Oxford Instruments Series 7 Cryostream low-temperature device. The temperature was stable to ±0.2 K and is considered accurate to ±0.5 K. Data were collected on a Nonius KappaCCD diffractometer, running under *COLLECT* software (Nonius, 1998). The *COLLECT* software calculates a strategy to optimize the goniometer and detector angular positions during data acquisition.

A total of 3861 image frames were obtained from 27 ω or φ scan sets (0.8 or 1.0° oscillation angles) using three different exposure times. The batch scaling factors showed no consistent variation with exposure time, indicating no significant sample decay. The scan sets with low detector θ offsets were measured first in the data collection strategy, in order to alleviate problems with ice rings which gradually build up during data collection. The high-angle images showed no evidence of contamination from ice rings. The unit-cell dimensions were determined by post-refinement of the setting angles of 97 904 reflections ($2.9 < \theta < 41.2°$) using the program *SCALEPACK* (Otwinowski & Minor, 1997). The cell errors obtained from this procedure are undoubtedly serious underestimates (Herbstein, 2000), but are used here in the absence of better estimates.

The image frames were integrated using *DENZO*(*SMN*) (Otwinowski & Minor, 1997). The resultant raw intensity files from *DENZO*(*SMN*) were processed using a locally modified version of *DENZOX* (Blessing, 1997*a*), which calculates direction cosines for the absorption correction, as well as applying rejection criteria on the basis of bad χ^2 values of the profile-fit and ignoring partial reflections at the starting or final frame of a scan set. A total of 358 895 intensity measurements, excluding space-group extinctions, were harvested from the image files. A semi-empirical absorption correction (Blessing, 1995) was applied to account for the absorption of the crystal and the mounting medium. The resulting data were sorted and merged using *SORTAV* (Blessing, 1997*b*), giving 23 246 independent data with a mean redundancy of 14.7 and to a resolution of $\sin(\theta_{\max})/\lambda = 1.079$ ($\theta_{\max} = 50^\circ$ for Mo $K\alpha$ radiation). A spherical-atom refinement using *SHELXL*97 (Sheldrick, 2008) was initially undertaken, with full-matrix least-squares on F^2 and using all the unique data with the weighting scheme $w = [\sigma(F_o)^2 + (AP)^2 + BP]^{-1}$, where $P = [F_o^2/3 + 2F_c^2/3]$ and $A = 0.0738$, $B = 0.2425$. All non-H atoms were allowed anisotropic thermal motion. Neutral atom scattering factors, coefficients of anomalous dispersion and absorption coefficients were as supplied in *SHELXL*97. Details of this refinement are given in Table 1. Displacement ellipsoid plots were obtained using the program *ORTEP*3 for *Windows* (Farrugia, 1997). All calculations were carried out using the *WinGX* package of crystallographic programs (Farrugia, 1999).

2.2. Multipole refinement

The multipole formalism of Hansen & Coppens (1978) as implemented in the *XD*2006 program suite (Volkov *et al.*, 2006) was applied. The aspherical atomic electron density $\rho(\mathbf{r})$ is given by

$$\rho(\mathbf{r}) = \rho_c(\mathbf{r}) + P_v\kappa^3\rho_v(\kappa\mathbf{r}) + \rho_d(\kappa'\mathbf{r}), \quad (1)$$

where ρ_c and ρ_v are the core and spherical valence densities, and

$$\rho_d(\kappa'\mathbf{r}) = \sum_{l=0}\kappa^3 R_l(\kappa'\mathbf{r})\sum_{m=0}^{l} P_{lm\pm}y_{lm\pm}(\mathbf{r}/r) \quad (2)$$

is the term accounting for the deformation valence densities. The $y_{lm\pm}$ are density-normalized real spherical harmonics and P_v, $P_{lm\pm}$ are the refinable populations. The function minimized in the least-squares procedure was $\Sigma w(|F_o| - k|F_c|)^2$, with only those reflections with $F > 3\sigma(F)$ included in the refinement. Each pseudoatom was assigned a core and spherical-valence scattering factor derived from the relativistic Dirac–Fock wavefunctions of Su & Coppens (1998) expanded in terms of the single-ζ functions of Bunge *et al.* (1993). The radial fit of these functions was optimized by refinement of the expansion–contraction parameter κ. The valence deformation functions for the non-H atoms used a single-ζ Slater-type radial function multiplied by the density-normalized spherical harmonics. The radial fits were optimized by refinement of their expansion–contraction parameters κ', a single parameter being used for each elemental type. The multipole expansion was truncated at the hexadecapole level for the non-H atoms, and at the quadrupole level for the H atoms. The C—H and O—H distances were set to the neutron diffraction determined averages for these types of bond (1.083 and 0.97 Å). An initial refinement using extensive chemical constraints with imposed *m* symmetry on all non-H atoms was used to determine the anisotropic displacement parameters (a.d.p.s) for the non-H atoms. These were then used to provide estimates of the H-atom a.d.p.s using the *SHADE* method of Madsen *et al.* (2004) and Madsen (2006), which has recently been shown (Munshi *et al.*, 2008) to provide accurate parameters. The calculated H-atom a.d.p.s were used in subsequent refinements as fixed parameters. In the final cycles of the refinement the chemical constraints were released, but the imposed *m* symmetry was retained for all C atoms. A satisfactory deconvolution of thermal motion was indicated by the fulfilment of the Hirshfeld (1976) mean-square displacement amplitude (m.s.d.a.) rigid-bond criterion for all those covalent bonds not involving H atoms. Thus, the largest Δ-m.s.d.a. was 6×10^{-4} Å^2 for the C31—C32 bond. Owing to the expected high correlations between the κ/κ' and multipole parameters, the former parameters were refined in separate blocks. In the final cycles, all parameters except κ/κ' were co-refined. No correlation matrix element greater than 0.75 was observed. A scatterplot of $F_{obs} - F_{calc}$ against $\sin(\theta)/\lambda$ (Fig. S1, supplementary data[1]) showed no discernable trend, indicating no scaling problems (Zhurov *et al.*, 2008). Residual density plots (Meindl & Henn, 2008) displayed in Fig. S2 (supplementary data) indicate that essentially no unmodelled features remain in the experimental data. The final refined multipole population parameters are given in Tables S1–S5 and representative residual, deformation and Laplacian maps shown in Figs. S8–S12 (supplementary data).

For a more direct comparison with the theoretical gas-phase integrated properties, the experimental integrated atomic properties were calculated for the free molecule 'extracted from the crystal' using the *TOPINT* routines of *XD*2006. The precision of numerical integration may be gauged from the value of the atomic Lagrangian $L(\Omega)$, which is proportional to the integrated flux of the gradient vector field of ρ at the interatomic surface, and should be equal to zero in the ideal case. In practice, a reasonable absolute value is considered to be $\sim 1 \times 10^{-3}$ a.u. or less (Volkov *et al.*, 2000). Several recent studies (Flensburg & Madsen, 2000; Volkov *et al.*, 2000) suggest a conservative estimate of *ca* ±5% for the accuracy of the integrated atomic properties; some properties, *e.g.* electron populations, are much less sensitive to errors than others.

Tables 2–4 list the topological parameters for the strong covalent, the weak intramolecular and the weak intramolecular interactions. The kinetic energy densities at the b.c.p.s $G(\mathbf{r})$ given in Tables 3 and 4 for the experimental densities

[1] Supplementary data for this paper are available from the IUCr electronic archives (Reference: PI5002). Services for accessing these data are described at the back of the journal.

were estimated using the functional approximation of Abramov (1997)

$$G(\mathbf{r}) = (3/10)(3\pi^2)^{2/3}\rho(\mathbf{r})^{5/3} + (1/6)\nabla^2\rho(\mathbf{r}), \quad (3)$$

while the corresponding potential energy densities at the b.c.p.s, $V(\mathbf{r})$, were obtained from the local virial relationship (expressed in a.u.) as shown by Bader (1990)

$$V(\mathbf{r}) = (1/4)\nabla^2\rho(\mathbf{r}) - 2G(\mathbf{r}). \quad (4)$$

The above approximation for $G(\mathbf{r})$ holds well for closed-shell interactions, where $\nabla^2\rho(\mathbf{r}) > 0$, and has been shown by Espinosa *et al.* (2001) to be an excellent approximation.

The experimental intermolecular interaction energies were calculated with the INTEREN option in *XD*2006 (Volkov *et al.*, 2006). The exact electrostatic term was obtained using the EP/MM method of Volkov *et al.* (2004), while the exchange-repulsion and dispersion terms were approximated by atom–atom potentials of Williams & Cox (1984). The experimental lattice energy was obtained in a similar fashion using the LATEN option.

2.3. Theoretical calculations

Gas-phase density-functional theory (DFT) calculations on (1) were undertaken with the *GAUSSIAN*03 program (Frisch *et al.*, 2004) using the B3LYP hybrid exchange-correlation functional (Stephens *et al.*, 1994; Becke, 1993, 1988; Vosko *et al.*, 1980; Lee *et al.*, 1988) and the 6-311++G(d, p) basis set (McLean & Chandler, 1980; Krishnan *et al.*, 1980; Clark *et al.*, 1983; Frisch *et al.*, 1984), which is of valence triple-ζ quality with one set of polarization and diffuse functions for all atoms, including hydrogen. We also used the *TURBOMOLE* program (TURBOMOLE, 2008; Ahlrichs *et al.*, 1989; Treutler & Ahlrichs, 1995; Eichkorn *et al.*, 1997; von Arnim & Ahlrichs, 1998) at the BLYP-D/TZVPP level. BLYP-D designates the BLYP gradient-corrected exchange-correlation functional (Becke, 1988; Lee *et al.*, 1988) supplemented by an empirical dispersion term (Grimme, 2004, 2006); TZVPP is a valence triple-ζ basis set with double polarization (Weigend & Ahlrichs, 2005; Weigend, 2006). The calculations in *TURBOMOLE* took advantage of the efficient RI (resolution of the identity) approximation for the evaluation of the Coulomb integrals (Eichkorn *et al.*, 1995*a*,*b*; Ahlrichs, 2004) within the multipole-accelerated RI scheme (Sierka *et al.*, 2003). It is important to note that standard exchange-correlation functionals are unable to account for the mainly dispersive intra- and especially intermolecular interactions that are in the focus of this study. This well documented deficiency (Zhao & Truhlar, 2006) has recently been largely overcome by the introduction of dispersion-corrected functionals of the type we have used herein (Grimme, 2004, 2006) that include a classical London dispersion term, and by functionals that were parameterized against a well balanced training set including weakly bound systems (Zhao & Truhlar, 2008). No correction was made for the basis-set superposition error (BSSE), as the dispersion corrected functionals have been parameterized without BSSE corrections. In any case the BSSE is expected to be very small, given that a TZVPP basis set was used.

Single-point calculations at the experimental geometry of the isolated molecule were performed. Geometry optimizations with B3LYP and BLYP-D gave significant differences from the experimental structure due to changes in the conformation of the CPh_2 unit. In turn this leads to somewhat different intramolecular interactions and as a consequence, the optimized structure is not considered further. However, we note that it is only ~ 17 kJ mol^{-1} more stable, a value quite commensurate with crystal packing effects. The final topological properties reported here were obtained at the experimental geometry. Topological analysis on the resultant wavefunction was undertaken using the programs *AIMPAC* (Biegler-König *et al.*, 1982) and *AIM*2000 (Biegler-König, 2000) and integrated properties and delocalization indices were calculated using *AIMall* (Keith, 2009). Gas-phase interaction energies between the dimeric pairs of (1) were calculated at the BLYP-D/TZVPP level.

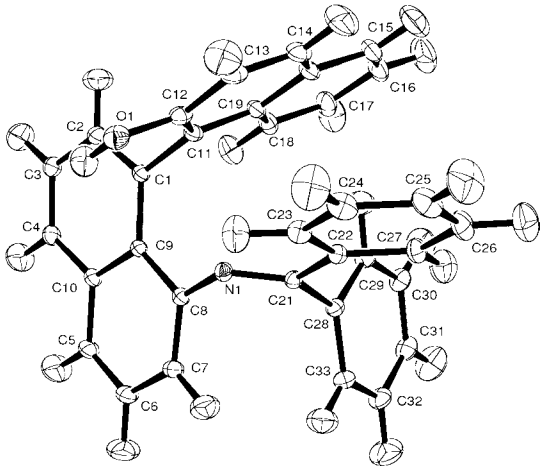

Figure 1
ORTEP view of (1) with 50% probability ellipsoids, showing the atomic labelling scheme. The label number for H atoms is the same as for their attached heavy atom.

3. Results and discussion

3.1. Description of the structure

An *ORTEP* view of (1), taken from the multipole refinement, is given in Fig. 1 and shows the atomic labelling scheme. Full details of bond lengths and angles are given in the supplementary data. The well established partial localization of double bonds was observed in the two naphthalene rings, with slightly shorter 1–2, 3–4, 5–6 and 7–8 C—C distances. The formal imine double bond N1═C21 = 1.2883 (2) Å is significantly shorter than the formal single bond N1—C8 = 1.4095 (2) Å, and the imine unit forms a nearly planar arrangement [maximum deviation of 0.042 (4) Å for N1 from mean plane]. Two of the three substituent benzene rings, C5—C10 and C28—C33, lie significantly out of the imine plane, with torsion angles C21—N1—C8—C7 = 68.7 (1) and N1—C21—C28—C29 = 97.5 (1)°, while the third ring, C22—C27, is

Table 2
Topological analysis of selected b.c.p.s in ρ.

Top line gives experimental values from this study, second line theoretical values from DFT (*GAUSSIAN*03) calculation. R_e: internuclear separation (Å); $d1$: $d1/2$ distance of b.c.p. from atoms 1/2 (Å); $\rho(\mathbf{r}_b)$: density (e Å^{-3}); $\nabla^2\rho(\mathbf{r}_b)$, λ_1, λ_2, λ_3: Laplacian and eigenvalues of Hessian (e Å^{-5}); ε: ellipticity; $\delta(\Omega_A, \Omega_B)$: delocalization index.

Bond	R_e	$d1$	$d2$	$\rho(\mathbf{r}_b)$	$\nabla^2\rho(\mathbf{r}_b)$	λ_1	λ_2	λ_3	ε	$\delta(\Omega_A, \Omega_B)$
N1—C8	1.4095 (2)	0.7897	0.6213	2.07	−16.30	−15.64	−15.04	14.39	0.04	–
		0.8496	*0.5612*	*1.98*	*−20.44*	*−14.47*	*−13.98*	*8.01*	*0.04*	*1.047*
N1—C21	1.2883 (2)	0.7985	0.4903	2.59	−29.42	−21.78	−17.61	9.97	0.24	–
		0.8234	*0.4656*	*2.47*	*−20.36*	*−19.72*	*−16.22*	*15.58*	*0.22*	*1.504*
C21—C22	1.4877 (2)	0.7524	0.7353	1.85	−15.16	−13.79	−12.32	10.95	0.12	–
		0.7545	*0.7332*	*1.78*	*−15.77*	*−12.92*	*−11.63*	*8.78*	*0.11*	*1.017*
C21—C28	1.4974 (2)	0.7680	0.7293	1.84	−15.00	−13.10	−12.88	10.98	0.02	–
		0.7595	*0.7379*	*1.76*	*−15.51*	*−12.26*	*−12.06*	*8.81*	*0.02*	*0.963*
C1—C11	1.4916 (2)	0.7521	0.7396	1.78	−13.49	−12.45	−11.99	10.95	0.04	–
		0.7513	*0.7404*	*1.74*	*−15.10*	*−11.86*	*−11.72*	*8.48*	*0.01*	*0.998*
O1—C12	1.3697 (3)	0.8704	0.4999	2.04	−19.84	−15.72	−14.78	10.66	0.06	–
		0.9021	*0.4678*	*1.90*	*−9.38*	*−13.52*	*−13.42*	*17.56*	*0.01*	*0.931*

close to coplanar, with a torsion angle of N1—C21—C22—C23 = 10.4 (1)°. On geometric grounds, therefore, there is the potential for π-delocalization between this latter ring and the imine group, which is discussed below.

Also of interest is the nature of the *peri* interaction in the 1,8-disubstituted naphthalene ring. The N1···C11 distance of 2.8018 (2) Å is considerably shorter than the sum of the van der Waals radii. Numerous structural determinations on 1,8-*X*,*Y* disubstituted naphthalenes have shown that, depending on the level of steric interactions between the *X* and *Y* groups, the aromatic ring system can undergo a significant C_2 distortion. The *X*,*Y* substituents move to opposite sides of the aromatic plane to alleviate the steric interactions. This distortion is conveniently described by the torsion angle *X*—C_{ipso}—C_{ipso}—*Y*, which is close to zero for the majority of structures in the Cambridge Crystallographic Database, but can reach 69.5° for extremely demanding *X*,*Y* substituents such as P(=S)PhBu^t (Omelanczuk *et al.*, 2003). Surprisingly, this distortion seems to be a rather soft mode, as clearly demonstrated by the case of 1-(*N*,*N*-dimethylamino)-8-nitronaphthalene (Egli *et al.*, 1986). There are three polymorphic forms with seven independent molecules, for which this torsion angle is different for each one and which varies from +1.19 to −27.1°. Likewise the crystal structure of 1,8-diiodonaphthalene (Bock *et al.*, 1998) contains six independent molecules, with different I—C_{ipso}—C_{ipso}—I torsion angles varying from +15.0 to −1.6°. In (1) itself, the torsion angle N1—C8—C1—C11 is 12.9 (1)°, which is not an unusual degree of distortion.

3.2. Molecular graph and π-delocalization

Topological analysis of both the experimental and theoretical densities leads to an identical molecular graph (*i.e.* topologically identical set of critical points and associated bond paths), as shown in Fig. 2. All the expected 63 b.c.p.s associated with the standard covalent bonds in (1) were found, including six (3,+1) ring c.p.s at the centroid of all benzenoid rings. In addition, four extra b.c.p.s were observed, owing to weak intramolecular interactions (§3.3 below), which in turn generate four more ring c.p.s. The experimental topological properties are listed in full in Table S6 (supplementary data), and selected properties are given in Table 2. The aromatic C—C and C—H bonds have the expected topological properties and merit no further comment. The more polar bonds in (1) (Table 2) show a typical discrepancy between theory and experiment, arising from well known causes which have been recently summarized by Koritsanszky (2006). The two imine nitrogen N—C bonds are clearly distinguished both in their lengths and also in their topological properties at the b.c.p.s. The Laplacian $-\nabla^2(\rho_r)$ map through the imine plane (Fig. 3*a*) clearly

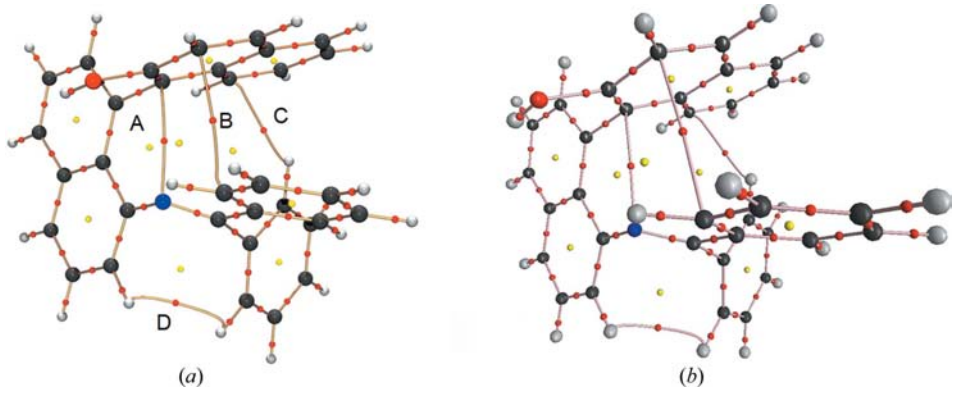

Figure 2
Molecular graph of (1) from the same viewpoint as Fig. 1, (*a*) experimental and (*b*) theoretical. The positions of the bond- and ring-critical points are shown as small red and yellow spheres. The weak intramolecular interactions are labelled A–D (see text).

shows three charge concentrations on the N1 atom, which are approximately coplanar with the substituent atoms, and which are consistent with an sp^2 hybridization for this atom (see §3.5).

As originally discussed by Bader and coworkers (Bader *et al.*, 1983; Cremer *et al.*, 1983), the preferential accumulation of charge due to π-bonding in organic molecules is most apparent by examination of the bond ellipticity ε, which is defined as $\lambda_1/\lambda_2 - 1$, where λ_1, λ_2 are the two negative eigenvalues of the Hessian matrix of the charge density. The major axis of ellipticity corresponds to the least negative eigenvalue λ_2 and this axis is normally aligned perpendicular to the π plane. For homopolar π bonds, the ellipticity at the b.c.p. is a good guide, but in general (and especially for heteropolar π bonds) it is more useful to examine the profile of ε along the whole bond path (Cheeseman *et al.*, 1998). The typical symmetric profiles for olefinic and aromatic C—C bonds given in this latter reference are also observed for all aromatic ring C—C bonds in (1) (see Fig. 4*f* and Fig. S3 in the supplementary data). Of particular importance is the orientation of the major axis of ellipticity with respect to the π plane, not just at the b.c.p., but also along the entire bond path. We define an angle $\varphi_{\rm ref}$ between the eigenvector of λ_2 and a reference vector normal to the π plane (usually taken as the normal to the best plane of those atoms involved in the localized or delocalized π system). For typical C—C aromatic bonds, ε is relatively large in the region near the b.c.p., and the angle $\varphi_{\rm ref}$ is close to zero (*i.e.* the two vectors are parallel). However, as the bond path approaches within ~ 0.2 Å of the nuclei, the value of ε falls to zero, or nearly zero, and the $\varphi_{\rm ref}$ angle abruptly flips to $\sim 90^\circ$, so that the major axis of ellipticity now lies in the π plane. This is due to the dominating influence of the charge concentrations in the valence-shell charge concentration (VSCC) of the C atoms (Cheeseman *et al.*, 1998). For heteropolar bonds, the value of ε at the b.c.p. may not even reflect the preferential accumulation plane of charge. Since the b.c.p. is shifted towards the most electropositive atom, the charge concentrations in the VSCC of that atom strongly influence the appearance of the ε profile. Scherer and co-workers have made extensive use of ellipticity profiles to describe π-delocalization effects in such diverse areas as *N*-heterocyclic carbenes (Tafipolsky *et al.*, 2002), agostic alkyl lithium complexes (Scherer *et al.*, 2002), β-agostic transition metal alkyls (Scherer *et al.*, 2003) and cyclopropenylidenes (Scherer *et al.*, 2008).

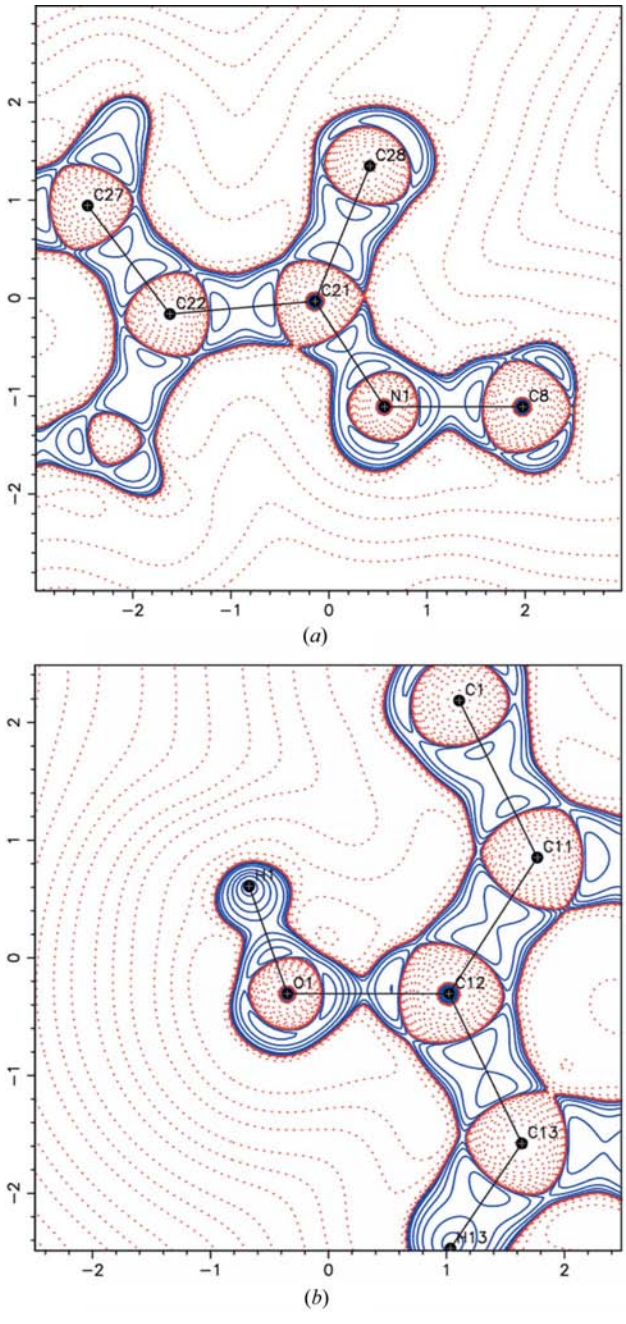

Figure 3
Experimental Laplacian $-\nabla^2\rho(\mathbf{r})$ of (1), (*a*) in the plane of the imine bond and (*b*) in the C—O—H plane. Contours are drawn at $\pm 2 \times 10^n$, $\pm 4 \times 10^n$ and $\pm 8 \times 10^n$ e Å^{-5} ($n = -3, -2, -1, 0, +1$): positive contours solid blue, negative contours in broken red. This figure is in colour in the electronic version of this paper.

The ellipticity profiles for the covalent bonds in the imine group are shown in Fig. 4 and are strikingly different. The asymmetric profile for the N1—C21 formal double bond shows the expected high degree of ellipticity at the b.c.p., with the $\varphi_{\rm ref}$ angle very close to zero and is qualitatively similar to the aromatic C—C bonds. Close to the nuclei, the $\varphi_{\rm ref}$ angle abruptly flips to $\sim 90^\circ$. The profile of the N1—C8 formal single bond, on the other hand, is fundamentally different. The ellipticity in the region of the b.c.p. is small, while the $\varphi_{\rm ref}$ angle is ~ 60–70°. The ellipticity rises in value when close to the N nucleus, where the $\varphi_{\rm ref}$ angle is $\sim 90^\circ$ and where the profile is dominated by the VSCC of the N atom. There is therefore no indication of any π character to this bond. Interestingly, the C21—C22 profile shows the classic appearance of an aromatic C—C bond, while the C21—C28 bond has a very low ellipticity on the region of the b.c.p. This implies a considerably greater π character in the former bond compared with the latter, despite the rather small differences in the C—C bond lengths and the topological properties at the b.c.p. given in Table 2 and the

Table 3
Topological properties of ρ_b for weak intramolecular interactions.

Top line gives experimental values from this study, second line theoretical values from DFT (*GAUSSIAN*03) calculation. R_e: internuclear separation (Å); $d1/2$: distance of b.c.p. from atoms 1/2 (Å); $\rho(\mathbf{r}_b)$: density (e Å^{-3}); $\nabla^2\rho(\mathbf{r}_b)$, λ_1, λ_2, λ_3: Laplacian and eigenvalues of Hessian (e Å^{-5}); $G(\mathbf{r}_b)$, $V(\mathbf{r}_b)$, $H(\mathbf{r}_b)$: in units of Hartree Å^{-3}; $G(\mathbf{r}_b)/\rho(\mathbf{r}_b)$: in units of Hartree e^{-1}.

Interacting atoms A, B	R_e	$d1$	$d2$	$\rho(\mathbf{r}_b)$	$\nabla^2\rho(\mathbf{r}_b)$	λ_1	λ_2	λ_3	ε	$G(\mathbf{r}_b)$	$G(\mathbf{r}_b)/\rho(\mathbf{r}_b)$	$V(\mathbf{r}_b)$	$H(\mathbf{r}_b)$	$\delta(\Omega_A, \Omega_B)$
C18···H29	2.6291	1.5841	1.0544	0.06	0.76	−0.14	−0.08	0.98	0.63	0.04	0.69	−0.03	0.01	–
		1.5814	*1.0531*	*0.07*	*0.74*	*−0.16*	*−0.07*	*0.97*	*1.29*	*0.04*	*0.65*	*−0.03*	*0.01*	*0.021*
N1···C11	2.8018 (2)	1.3734	1.4428	0.11	1.22	−0.32	−0.18	1.72	0.83	0.08	0.70	−0.07	0.01	–
		1.3870	*1.4357*	*0.10*	*1.23*	*−0.29*	*−0.17*	*1.68*	*0.67*	*0.07*	*0.71*	*−0.06*	*0.01*	*0.054*
C13···C23	3.2286 (2)	1.6091	1.6237	0.05	0.49	−0.10	−0.07	0.66	0.44	0.03	0.57	−0.02	0.01	
		1.6048	*1.6267*	*0.05*	*0.49*	*−0.08*	*−0.06*	*0.64*	*0.34*	*0.03*	*0.59*	*−0.02*	*0.01*	*0.028*
H7···H33	2.1988	1.0745	1.2394	0.05	0.76	−0.18	−0.07	1.02	1.39	0.04	0.78	−0.03	0.01	–
		1.0997	*1.1886*	*0.06*	*0.74*	*−0.19*	*−0.10*	*1.03*	*1.00*	*0.04*	*0.69*	*−0.03*	*0.01*	*0.018*

virtually identical Laplacian features (Fig. 3). These π delocalization effects are clearly related to the N—C—C—C torsion angles of the phenyl rings relative to the plane of the imine group, which were discussed in §3.1. The ellipticity profiles of the experimental charge density reveal subtle π delocalization effects and strongly imply there is only a significant π delocalization between the imine group and the C22—C27 benzene ring, which is close to coplanar with it.

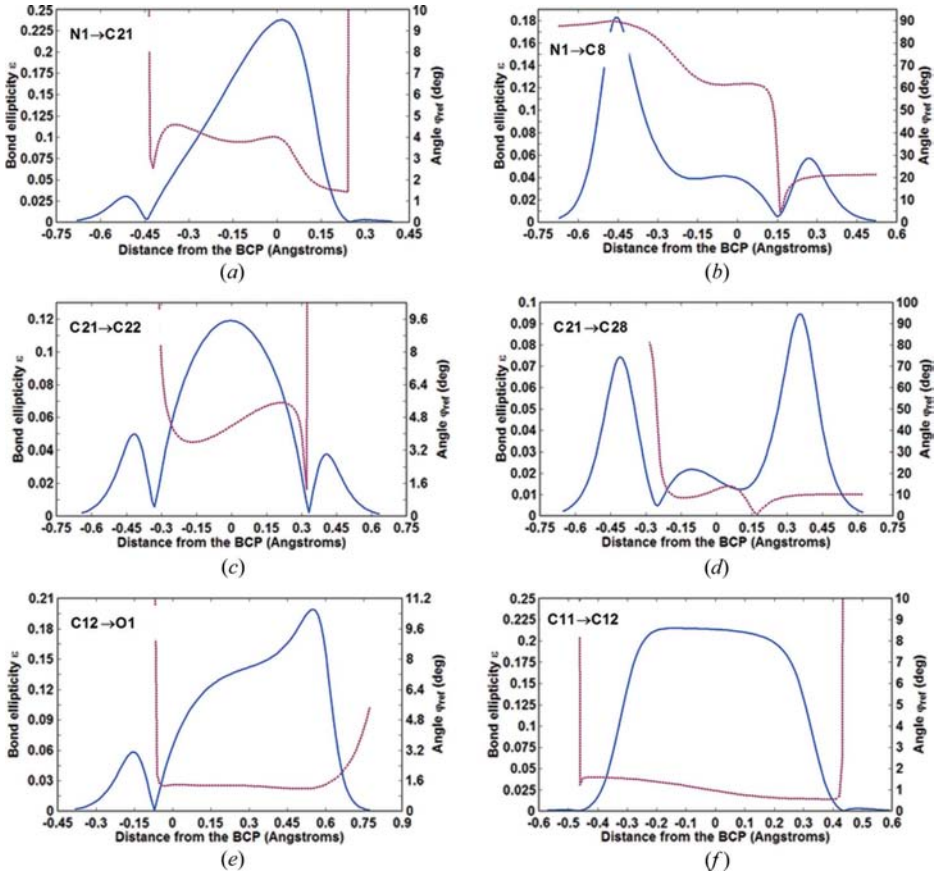

Figure 4
Plots of the bond ellipticities ε along the bond path (solid blue line) with the φ_{ref} angle (dotted violet line). For plots (*a*)–(*d*) the reference vector (see text) is normal to the C8—N1—C21—C22—C28 mean plane, while for (*e*) and (*f*) it is normal to the C_6 ring containing C11 and C12. This figure is in colour in the electronic version of this paper.

3.3. Intramolecular interactions

There are four intramolecular contacts shorter than the sum of the van der Waals radii that give rise to b.c.p.s between the atomic centres. These comprise the N···C *peri* interaction (Balasubramaniyan, 1966) between N1 and C11, a C···C π-stacking interaction between C13 and C23, a CH···π interaction (Nishio *et al.*, 1998) between H29 and C18, and a H···H interaction (Matta, 2006) between H7 and H33. These are shown in Fig. 2 and are labelled A–D. The experimental and theoretical topological properties at the b.c.p.s for these weak interactions are given in Table 3. In all cases, agreement between experiment and theory is excellent. These weak interactions are characterized by very small values of $\rho(\mathbf{r})$, small positive values of $\nabla^2\rho(\mathbf{r}_b)$, high values of ε and λ_3 (relative to $\lambda_{1,2}$), nearly zero values of $H(\mathbf{r}_b)$ and values of $|V(\mathbf{r}_b)|/G(\mathbf{r}_b)$ generally ≤ 1. In terms of the Espinosa classification (Espinosa *et al.*, 2002), these weak interactions (and the intramolecular ones discussed below) overlap between the type I pure closed-shell zone and the type II transit zone. The high values for the ellipticity are due to the relatively low value of λ_2 and cannot be ascribed to any π bonding. In addition, their ellipticity profiles (Fig. S4, supplementary data) do not resemble those for genuine π-bonded interactions, but show striking variations, including discontinuities where the structure of the Hessian changes. The delocalization indices (Bader & Stephens, 1975) between the inter-

acting atoms are all very small, the largest one being for $\delta(\Omega_{N1}, \Omega_{C11})$ = 0.054. This indicates a very low level of electron sharing between the atomic centres involved.

The charge-density investigation confirms the presence of an intramolecular CH$\cdots\pi$ interaction, which was initially suspected on geometric grounds (Vyskočil *et al.*, 2002). The H29$\cdots$C contacts for the benzene ring are in the narrow range 2.629–2.908 Å (Fig. S5, supplementary data), but it is only the shortest one, H29$\cdots$C18, which actually generates a bond path. The Koch & Popelier (1995) criteria for hydrogen bonds are difficult to apply in full for experimental charge densities, but the first four relating to the presence of a bond path, the magnitudes of $\rho(\mathbf{r})$ and $\nabla^2\rho(\mathbf{r}_b)$ and the mutual interpenetration are clearly fulfilled.

The *peri*-*X*—*Y* interaction in 1,8-disubstituted naphthalenes has been known for a long time (Balasubramaniyan, 1966) and is of interest because the enforcing geometry results in a close interatomic *X*$\cdots$*Y* contact, which is much shorter than the sum of the van der Waals radii for all atoms other than H. This provides an ideal environment in which to examine interesting weak interactions such as the 'N$\Rightarrow$Si/P donor–acceptor interaction' (which potentially involves hypercoordination at the Si/P atom; see, for example, Schiemenz & Näther (2002), Dominiak *et al.* (2005) and refs therein, and O'Leary & Wallis (2006). In terms of characterizing such interactions by AIM methods, the most important evidence lies in the presence or absence of a bond path (Bader, 1998). An experimental charge-density study on naphthalene itself (Oddershede & Larsen, 2004) revealed no such 1,8 H$\cdots$H intramolecular bond path, but in both 1,8-bis(*N*,*N*-dimethylamino)naphthalene (Mallinson *et al.*, 1999) and 8-(*N*,*N*-dimethylamino)-naphthyl-1-carboxamide (Lyssenko *et al.*, 2004) a bond path connecting the 1,8 interacting atoms was experimentally observed. The presence of a 1,8-*peri* bond path seems rather ubiquitous; our DFT calculations based on the experimental structures of 1-trifluorosilyl-8-(*N*,*N*-dimethylamino)naphthalene (Carre *et al.*, 1994) and 1,8-difluoronaphthalene (Meresse *et al.*, 1975) also reveal a 1,8-bond path for both species. In the case of 8-(*N*,*N*-dimethylamino)naphthyl-1-carboxamide, the 1,8 interaction could be realistically viewed as an incipient nucleophilic attack by the nitrogen lone pair at the carbonyl group (Lyssenko *et al.*, 2004), and a similar interpretation is also appropriate for the strong 1,8 interaction found in 1-trifluorosilyl-8-(*N*,*N*-dimethylamino)naphthalene (Carre *et al.*, 1994). However, it is clearly inappropriate to attribute a 1,8 donor–acceptor interaction in 1,8-bis(*N*,*N*-dimethylamino)naphthalene (Mallinson *et al.*, 1999), as both substituents possess a lone pair. This lone pair–lone pair interaction should be destabilizing, nevertheless, a bond path is observed both in experiment and in our DFT calculations.

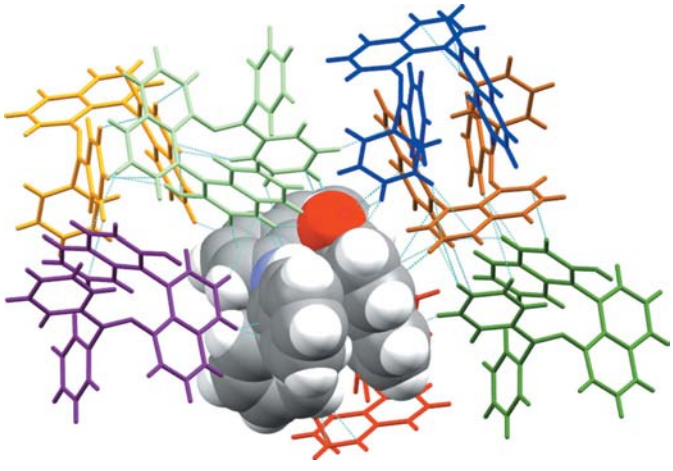

Figure 5
Disposition of the seven molecules that give rise to the unique intermolecular interactions in the crystal structure of (1). Symmetry operations: (i) pale green $(1-x, \frac{1}{2}+y, \frac{1}{2}-z)$; (ii) red $(-x, -y, -z)$; (iii) purple $(x, \frac{1}{2}-y, \frac{1}{2}+z)$; (iv) blue $(1+x, y, z)$; (v) dark green $(x, -\frac{1}{2}-y, z-\frac{1}{2})$; (vi) orange $(x, 1+y, z)$; (vii) brown $(1-x, -y, -z)$.

Likewise, in (1) the N1$\cdots$C11 1,8 interaction cannot be viewed as a donor–acceptor type. The N1 atom has only three charge concentrations in the VSCC, see §3.5. There is a charge-depletion facing atom C11. Likewise, the C11 atom has three charge concentrations in the VSCC and a (3,−1) saddle point faces the N1 atom. The *peri* interaction may be similar to the π–π stacking interaction commonly seen in aromatic systems (Munshi & Guru Row, 2006), although in this case the separation of the two atoms is much shorter, leading to a stronger interaction. The recent re-interpretation by Pendás *et al.* (2007) of the significance of the bond path as a path of privileged exchange may also be of relevance in this case. We note that 1,8-diphosphorus-substituted naphthalenes can show high through-space $^4J(^{31}P–^{31}P)$ NMR couplings (Kilian *et al.*, 2004).

The nearly identical charges on H7 and H33 imply that their observed interaction is of the H$\cdots$H type recently reviewed by Matta (2006). The chemical significance of the bond path between these types of interacting H atoms is a controversial topic. Matta *et al.* (2003), Hernández-Trujillo & Matta (2007) and Bader (2006) have strongly argued that the H$\cdots$H interaction in molecules such as phenanthrene or biphenyl is a stabilizing one, while Poater *et al.* (2006*a*,*b*) have taken the opposite view. Recently Grimme *et al.* (2009) have concluded from IR studies on selectively deuterated phenanthrene that the H$\cdots$H interaction corresponds to a repulsive part of the potential, although this is disputed by Bader (2009). Regardless of these differences of interpretation, we can categorically state that the intramolecular H$\cdots$H bond path in (1) is a robust topological object, unambiguously present in both the experimental and theoretical molecular graphs (see Fig. 2). The interaction of the b.c.p. with the associated ring c.p. is not sufficiently strong to lead to a catastrophic situation (Bader, 1990). Moreover, exactly the same graph, including a H$\cdots$H interaction line, is observed in the topology of the potential energy density (virial) field $V(\mathbf{r})$ of (1) (see Fig. S5, supplementary data). As stated by Bader (1998), the presence of an interaction line in the virial field, *i.e.* where the potential energy density is maximally negative and maximally stabilizing with respect to neighbouring lines, implies the H$\cdots$H interaction is a stabilizing one. Since the molecular graph and the virial graph are normally homeomorphic (Keith *et al.*,

Table 4
Topological properties of ρ_b for the unique intermolecular interactions.

Top line gives experimental values, second line theoretical values from a DFT-D (*TURBOMOLE*) calculation. Some c.p.s were not observed in the theoretical density (n.a.). Type: I CH···C(π), II CH···N(π), III CH···O, IV OH···C(π), V CH···HC; R_e: internuclear separation (Å); *d*1/2: distance of b.c.p. from atoms 1/2 (Å); $\rho(\mathbf{r}_b)$: density (e Å^{-3}); $\nabla^2\rho(\mathbf{r}_b)$, λ_1, λ_2, λ_3: Laplacian and eigenvalues of Hessian (e Å^{-5}); $G(\mathbf{r}_b)$, $V(\mathbf{r}_b)$, $H(\mathbf{r}_b)$: in units of Hartree Å^{-3}.

Interacting atoms A, B	Type	R_e	D—H···A (°)	*d*1	*d*2	$\rho(\mathbf{r}_b)$	$\nabla^2\rho(\mathbf{r}_b)$	λ_1	λ_2	λ_3	ε	$G(\mathbf{r}_b)$	$G(\mathbf{r}_b)/\rho(\mathbf{r}_b)$	$V(\mathbf{r}_b)$	$H(\mathbf{r}_b)$
C3···H25^{i}	I	2.663	153.4	1.6071	1.0560	0.06	0.50	−0.16	−0.13	0.80	0.27	0.03	0.53	−0.03	0.00
				1.6283	*1.0524*	*0.06*	*0.58*	*−0.17*	*−0.08*	*0.82*	*1.18*	*0.03*	*0.61*	*−0.03*	*0.01*
C7···H13^{i}	I	2.869	152.1	1.7189	1.1629	0.04	0.29	−0.12	−0.11	0.51	0.14	0.02	0.45	−0.01	0.00
				1.7086	*1.1623*	*0.03*	*0.35*	*−0.08*	*−0.07*	*0.51*	*0.13*	*0.02*	*0.57*	*−0.02*	*0.01*
C10···H24^{i}	I	2.903	127.9	1.8493	1.1710	0.03	0.32	−0.09	−0.03	0.44	2.03	0.02	0.58	−0.01	0.01
				1.7122	*1.1906*	*0.04*	*0.41*	*−0.08*	*−0.05*	*0.53*	*0.62*	*0.02*	*0.62*	*−0.02*	*0.01*
N1···H14^{i}	II	2.809	135.5	1.6546	1.1655	0.03	0.42	−0.10	−0.07	0.59	0.47	0.02	0.66	−0.02	0.01
				1.6782	*1.1353*	*0.04*	*0.45*	*−0.11*	*−0.09*	*0.65*	*0.15*	*0.03*	*0.62*	*−0.02*	*0.01*
O1···H14^{i}	III	2.536	146.7	1.5033	1.0418	0.05	0.70	−0.16	−0.15	1.01	0.05	0.04	0.76	−0.03	0.01
				1.5043	*1.0323*	*0.06*	*0.69*	*−0.18*	*−0.18*	*1.04*	*0.02*	*0.04*	*0.70*	*−0.03*	*0.01*
H1···C25^{i}	IV	2.693	147.5	1.0151	1.6812	0.03	0.33	−0.10	−0.08	0.51	0.28	0.02	0.53	−0.01	0.00
				1.0226	*1.6780*	*0.04*	*0.45*	*−0.12*	*−0.08*	*0.65*	*0.54*	*0.03*	*0.59*	*−0.02*	*0.01*
H23···H14^{i}	V	2.111	–	1.0468	1.0719	0.05	0.51	−0.22	−0.17	0.91	0.33	0.03	0.56	−0.02	0.01
				1.0241	*1.0951*	*0.06*	*0.61*	*−0.20*	*−0.18*	*0.98*	*0.13*	*0.04*	*0.64*	*−0.03*	*0.01*
C3···H30^{ii}	I	2.671	135.5	1.6427	1.0867	0.06	0.45	−0.21	−0.13	0.79	0.60	0.03	0.47	−0.03	0.00
				1.6090	*1.0657*	*0.06*	*0.57*	*−0.16*	*−0.10*	*0.82*	*0.58*	*0.03*	*0.60*	*−0.03*	*0.01*
C5···H16^{ii}	I	3.099	131.6	1.7867	1.3329	0.02	0.25	−0.05	−0.05	0.35	0.16	0.01	0.59	−0.01	0.00
				1.6760	*1.2804*	*0.02*	*0.26*	*−0.06*	*−0.04*	*0.36*	*0.37*	*0.01*	*0.59*	*−0.01*	*0.00*
C5···H17^{ii}	I	3.310	122.8	1.9876	1.3274	0.02	0.23	−0.01	−0.01	0.25	0.39	0.01	0.73	−0.01	0.00
				n.a											
C9···H17^{ii}	I	3.336	151.7	2.0377	1.3175	0.02	0.18	−0.02	0.00	0.21	3.04	0.01	0.60	−0.01	0.00
				n.a.											
H18···C30^{ii}	I	2.663	140.9	1.0460	1.5081	0.05	0.54	−0.15	−0.10	0.79	0.57	0.03	0.65	−0.02	0.01
				1.0783	*1.5389*	*0.05*	*0.57*	*−0.15*	*−0.09*	*0.80*	*0.73*	*0.03*	*0.63*	*−0.03*	*0.01*
N1···H3^{iii}	II	3.267	145.8	1.9020	1.3703	0.02	0.19	−0.03	−0.02	0.24	0.43	0.01	0.59	−0.01	0.00
				n.a.											
C22···H4^{iii}	I	2.645	136.8	1.6235	1.0558	0.07	0.55	−0.22	−0.11	0.89	0.96	0.03	0.52	−0.03	0.00
				1.6146	*1.0457*	*0.06*	*0.62*	*−0.18*	*−0.09*	*0.89*	*0.90*	*0.04*	*0.61*	*−0.03*	*0.01*
C23···H3^{iii}	I	3.019	113.7	1.7628	1.3179	0.03	0.36	−0.05	−0.03	0.44	1.00	0.02	0.71	−0.01	0.01
				1.7248	*1.3119*	*0.03*	*0.36*	*−0.06*	*−0.03*	*0.45*	*0.70*	*0.02*	*0.65*	*−0.01*	*0.01*
O1···H31^{iv}	III	2.501	129.5	1.4660	1.0380	0.06	0.79	−0.21	−0.15	1.15	0.43	0.04	0.78	−0.03	0.01
				1.4784	*1.0265*	*0.06*	*0.83*	*−0.21*	*−0.18*	*1.22*	*0.15*	*0.05*	*0.76*	*−0.04*	*0.01*
O1···H32^{iv}	III	2.837	115.7	1.6298	1.2501	0.02	0.45	−0.07	−0.02	0.55	2.02	0.02	1.01	−0.01	0.01
				1.6172	*1.2470*	*0.03*	*0.46*	*−0.09*	*−0.05*	*0.59*	*0.96*	*0.03*	*0.76*	*−0.02*	*0.01*
C17···H26^{v}	I	2.794	155.9	1.6806	1.1279	0.04	0.42	−0.12	−0.06	0.61	0.91	0.02	0.60	−0.02	0.01
				1.6794	*1.1249*	*0.04*	*0.42*	*−0.11*	*−0.07*	*0.60*	*0.77*	*0.02*	*0.58*	*−0.02*	*0.01*
H5···H16^{vi}	V	2.251	–	1.1683	1.0930	0.03	0.60	−0.09	−0.05	0.75	0.86	0.03	1.03	−0.02	0.01
				1.1522	*1.1125*	*0.05*	*0.53*	*−0.15*	*−0.14*	*0.82*	*0.11*	*0.03*	*0.64*	*−0.02*	*0.01*
H6···H16^{vi}	V	2.539	–	1.4203	1.2131	0.02	0.38	−0.05	−0.01	0.43	4.72	0.02	0.88	−0.01	0.01
				n.a.											
H2···C12^{vii}	I	2.929	145.9	1.1548	1.8070	0.03	0.35	−0.10	−0.05	0.50	0.89	0.02	0.56	−0.01	0.01
				1.1639	*1.7948*	*0.04*	*0.36*	*−0.10*	*−0.05*	*0.51*	*0.95*	*0.02*	*0.58*	*−0.02*	*0.01*
H3···C14^{vii}	I	2.866	140.5	1.1401	1.7907	0.03	0.42	−0.09	0.06	0.57	0.59	0.02	0.66	−0.02	0.01
				1.1374	*1.7716*	*0.04*	*0.42*	*−0.16*	*−0.07*	*0.60*	*0.67*	*0.02*	*0.57*	*−0.02*	*0.01*

Symmetry operators: (i) $1-x, \frac{1}{2}+y, \frac{1}{2}-z$; (ii) $-x, -y, -z$; (iii) $x, \frac{1}{2}-y, \frac{1}{2}+z$; (iv) $1+x, y, z$; (v) $x, -\frac{1}{2}-y, z-\frac{1}{2}$; (vi) $x, 1+y, z$; (vii) $1-x, -y, -z$.

1996), which is the case for (1), then the atomic interaction lines in the molecular graph indicate stabilizing interactions.

3.4. Intermolecular interactions

Despite the presence of a hydroxyl group, there are no conventional OH···O or OH···N hydrogen bonds observed in the crystal packing of (1), which is dominated by weaker interactions. Examination of the closest-neighbour molecules (Fig. 5) reveals 22 unique intermolecular atomic contacts, from seven independent dimeric pairs of (1), which give rise to bond paths between the atomic centres. These comprise 13 CH···C(π) interactions, two CH···N(π), one OH···C(π), three CH···HC interactions and three CH···O interactions,

Table 5
Experimental intermolecular interaction energies (kJ mol^{-1}) from multipole populations.

Dimeric pairs†	E_{int}	E_{es}	$E_{ex\text{-}rep}$	E_{disp}	E_{int}(DFT)‡
i	−62.2	−33.0	44.7	−73.9	−44.9 (−60.9)
ii	−99.8	−53.1	55.8	−102.5	−51.9 (−86.7)
iii	−28.3	−10.8	18.0	−35.5	−19.5 (−29.8)
iv	−19.3	−13.3	11.9	−17.9	−11.0 (−14.3)
v	−17.0	−6.7	5.9	−16.2	−10.7 (−13.9)
vi	−5.1	0.6	8.9	−14.6	−7.8 (−12.9)
vii	−41.8	−15.2	20.9	−47.5	−29.8 (−41.0)

† See Table 4 for symmetry operators generating the second molecule. ‡ Theoretical value from DFT-D *TURBOMOLE* calculations; empirical dispersive energy corrections given in parentheses.

which are shown schematically in Fig. S6 (supplementary data). The experimental and theoretical topological properties are listed in Table 4 and they show the same features as mentioned above for the weak intramolecular interactions. Some weak interactions were not observed in the theoretical density. The mean C—H···C(π) angle of 139.1° (range 113.7–155.9°) suggests a strong directionality for these weak hydrogen bonds, which is close to the value found by Steiner & Desiraju (1998) for CH···O bonds. This implies that simply the presence of a bond path alone is a sufficient criterion to distinguish true hydrogen bonds from van der Waals interactions, as indeed was found by Gatti *et al.* (2002) for CH···O bonds.

One striking way of visualizing the inter-atomic interactions in crystal packing is through Hirshfeld surface plots (Spackman & Jayatilaka, 2009). These plots provide a unique signature for a molecule in a crystal and, as they depend on the crystalline environment, they may be different for the same molecule in different crystal environments. The Hirshfeld surface for (1) is shown in Fig. 6(*a*). This surface is mapped by the geometric function d_{norm} (Spackman & Jayatilaka, 2009), which takes into account the differing sizes of atoms

$$d_{norm} = \frac{d_i - r_i^{vdW}}{r_i^{vdW}} + \frac{d_e - d_e^{vdW}}{r_e^{vdW}}, \qquad (5)$$

where $d_{i/e}$ is the distance from the surface to the nearest interior/exterior atom, $r_{i/e}^{vdW}$ is the corresponding van der Waals radius. Contact zones shorter than the sum of the van der Waals radii are shown as red areas in these plots. Analysis of the corresponding fingerprint plot, Fig. 6(*b*), shows that it is dominated by the CH···C(π) and CH···HC interactions, as expected for a molecule that is primarily constituted of aromatic rings. It is also immediately evident that there are no significant $\pi\cdots\pi$ stacking interactions in the crystal structure of (1) (typical of polycyclic aromatic compounds, see McKinnon *et al.*, 2004), as the characteristic central marker (Spackman & Jayatilaka, 2009) is lacking in the fingerprint plot.

In order to examine the relationship between pairs of molecules as defined by their individual atom–atom (bond path) interactions described above, and their overall interaction energy, we have computed the latter from the experimental charge density and by DFT calculations at the BLYP-D/TZVPP level. The total interaction energy between two closed-shell molecules may be expressed as the sum of electrostatic, exchange-repulsion, dispersion and induction terms (Stone, 1996).

$$E_{int} = E_{es} + E_{ex-rep} + E_{disp} + E_{ind} \qquad (6)$$

For an experimental electron distribution obtained from the multipole model, it may be assumed that the induction effects are already included in the pseudo-atom model. The experimental interaction energies for each of the seven unique pairs of molecules are given in Table 5. It can be seen that the interaction energy is, for the most part, determined by the dispersion term, as the electrostatic and exchange-repulsion contributions are almost equal and of opposite signs. The only case for which this is not so is (vi), which involves only weak CH···HC interactions. The agreement between the experimental and theoretical energies is qualitatively reasonable, although the experimental energies are in general larger. Nevertheless, the ordering of energies for the seven dimeric-pair interactions is identical and the overall interaction energies for each pair are clearly related in a qualitative sense with the number of intermolecular bond paths. The lattice energy of (1) is computed as −274.2 kJ mol^{-1}, which is probably an overestimate for a molecule of this type.

3.5. Atomic polarizations and integrated properties

The atomic polarizations that occur on chemical bonding are of fundamental interest to chemists, but unfortunately the concept of atomic charges has proved difficult to quantify accurately. QTAIM atomic charges are physically well defined and are obtained by numerical integration of the electron population over the volume enclosed by the zero-flux surface of each atom (the atomic basin). They generally lead to larger charges than other partitioning methods (Bader & Matta, 2004), but have the considerable advantage that a direct comparison is possible between experiment and theory. The molecular dipole moment for (1) is calculated to be 6.89 D from the experimental multipole populations. The charges for

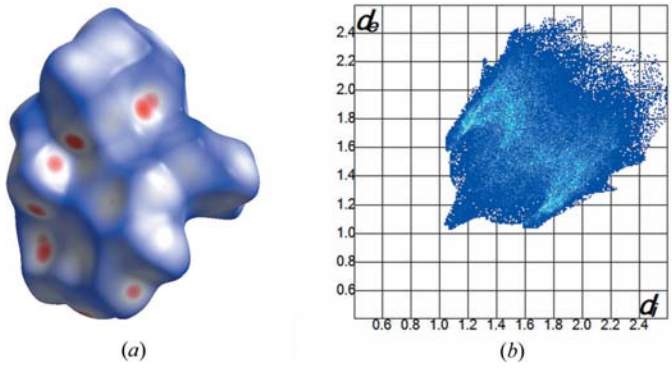

Figure 6
(*a*) Hirshfeld surface of (1) mapped with d_{norm} over the range −0.24 to 1.3; (*b*) fingerprint plot of the Hirshfeld surface.

Table 6
Atomic charges.

Atom	$q(Pv)$†	q(stock)‡	$q(\Omega)_{exp}$§	$q(\Omega)_{theo}$§
O1	−0.219 (10)	−0.228	−1.194	−1.089
N1	−0.101 (11)	−0.145	−0.996	−1.104
Cs8	−0.123 (16)	−0.023	0.236	0.346
C12	−0.104 (17)	0.022	0.440	0.506
C21	−0.009 (14)	0.074	0.580	0.653
C_{phenyl} av.	−0.046	−0.047	−0.069	−0.013
$C_{naphthyl}$ av.	−0.054	−0.054	−0.086	−0.015
H1	0.158 (9)	0.186	0.661	0.569
H_{phenyl} av.	0.078	0.071	0.112	0.022
$H_{naphthyl}$ av.	0.078	0.075	0.122	0.028
Sum over all atoms	0.000	0.000	0.020	0.000

† From multipole populations. ‡ From integration over stockholder partitioned atoms. § From integration over atomic basins.

selected atoms are given in Table 6, full lists of atomic charges and other integrated properties are given in Tables S7 and S8 (supplementary material). The stockholder charges q(stock), obtained by integration of the electron density partitioned according to the Hirshfeld method (Hirshfeld, 1977), are also given for comparison.

There is reasonably good agreement between the different charge-partitioning methods. The aromatic C and H atoms bear slightly negative and positive charges, except those atoms (C8 and C12) bonded to the O or N atoms that bear positive charges. The imine carbon C21 also has a significant positive charge. The atomic volumes for these positively charged C atoms, and also the other quaternary aromatic C atoms are noticeably smaller than for the other C atoms. As expected, the electronegative N and O atoms carry a substantial negative charge, especially in the QTAIM charges. The loss of charge for the H atoms involved in the hydrogen bonds (Koch & Popelier, 1995) is expected to be very small for the weak interactions reported here, and indeed it is not detectable. The mean (theoretical) charge on the aromatic H atoms involved in weak hydrogen bonds is +0.020, while it is +0.027 for those H atoms not involved. The corresponding values from experiment (+0.114 and +0.121) show the same trend.

The imprint of chemical bonding is also manifested in the polarizations that occur in the atomic valence-shell charge concentrations (VSCC), these being most succinctly described in terms of the critical points in the negative Laplacian $-\nabla^2\rho(\mathbf{r})$ (*i.e.* the atomic graph). This graph is a [V,E,F] polyhedron satisfying Euler's rule, such that V + F − E = 2 and where the vertices (V) are the (3, −3) c.p.s of charge concentration, the edges (E) the saddle point (3,−1) c.p.s and the faces (F) the (3,+1) c.p.s of charge depletion (Bader, 1990). The atomic graphs and corresponding Laplacian isosurface plots of the N1 and O1 atoms are shown in Fig. 7. The N1 atom has the form [3,4,3], with a trigonal arrangement of three (3, −3) c.p.s, two of which are associated with covalent bonds and the third with the formal lone pair. Above and below the trigonal plane are two charge depletions, which are consistent with a formal sp^2 hybridization and a partially occupied p_z orbital. The sp^2 hybridized C atoms in the aromatic rings have similar, but more extended, graphs of the [3,5,4] form. While the Laplacian distribution around the O1 atom seen in Fig. 3 is deceptively similar to that of N1, the atomic graph is quite different, with the form [4,5,3] where the four charge concentrations have an approximate tetrahedral arrangement. The two charge concentrations associated with the lone pairs are almost merged into one and the saddle point (3, −1) c.p. has almost the same density, as has been similarly reported for the tyrosine hydroxyl O atom (Zarychta *et al.*, 2007). An sp^3 description seems most appropriate for the hybridization of this atom, but interestingly the ellipticity profile along the C12—O1 bond suggests some π character, implying sp^2 hybridization. While the ellipticity at the b.c.p. is very small, the value of ε rises considerably on approaching the O1 atom and the φ_{ref} angle is close to zero along most of the path, which is typical of the π bonds described above.

4. Conclusions

The weak intra- and intermolecular C···N, CH···X, OH···C and H···H interactions in (1) have been characterized through their charge-density properties. The *peri*-1,8 C···N interaction is at the strong end of the spectrum of these interactions, owing to the enforced short contact distance. In the case of (1), the resultant bond path cannot be associated with a donor ⇒ acceptor interaction. There are seven dimeric pairs associated with the unique set of intermolecular interactions in the crystal phase and their interaction energies obtained from the multipole populations and by DFT-D calculations show a clear correspondence with the number of intermolecular bond paths. A comparison of the ellipticity profiles along the C21—C22 and C21—C28 bond paths clearly shows π-delocalization with the imine double bond for the former but not the latter, which is not evident in the topolo-

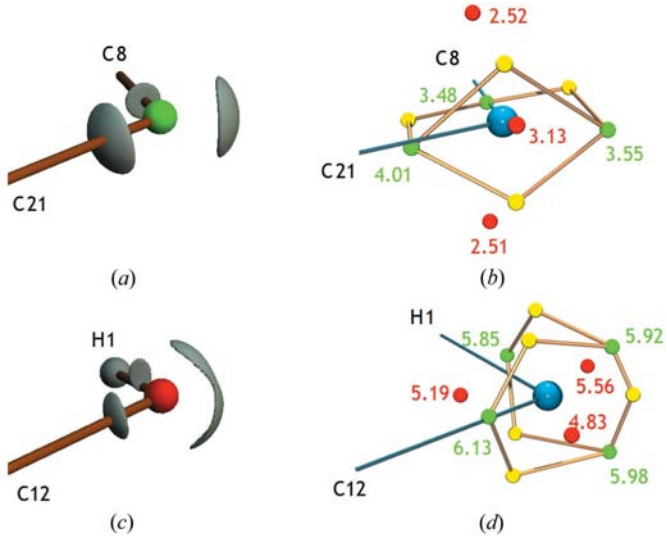

Figure 7
(*a*) Isosurface (50 e Å^{-5}) of negative Laplacian in VSCC of atom N1; (*b*) atomic graph of the N1 atom; (*c*) isosurface (110 e Å^{-5}) of negative Laplacian in VSCC of the O1 atom; (*d*) atomic graph of atom O1. The (3,−3), (3,−1) and (3,+1) critical points are colour coded as green, yellow and red, and charge densities (e Å^{-3}) are given in the same colour.

gical properties or the Laplacian maps. Despite the reservations expressed by Koritsanszky (2006) regarding the uncertainties in X-ray derived charge densities and the reliability of derived bond-topological properties, agreement between experimental and theoretical topological parameters for the weak interactions reported herein is in general quite satisfactory. The absolute values for $\rho(\mathbf{r})$ and $\nabla^2\rho(\mathbf{r}_b)$ in Tables 3 and 4 are quite small, and the small absolute differences may be a result of fortuitous cancellation of errors.

We thank the EPSRC for grant GR/M91433 towards the purchase of a KappaCCD diffractometer and NATO for a fellowship to ŠV (administered by the Royal Society of Chemistry). We also thank Professor J. McGrady for access to the FATCAT computing cluster facility.

References

Abramov, Yu. A. (1997). *Acta Cryst.* A**53**, 264–272.
Ahlrichs, R. (2004). *Phys. Chem. Chem. Phys.* **6**, 5119–5121.
Ahlrichs, R., Bär, M., Häser, M., Horn, H. & Kölmel, C. (1989). *Chem. Phys. Lett.* **162**, 165–169.
Arnim, M. von & Ahlrichs, R. (1998). *J. Comput. Chem.* **19**, 1746–1757.
Bader, R. F. W. (1990). *Atoms in Molecules: A Quantum Theory*. Oxford: Clarendon Press.
Bader, R. F. W. (1998). *J. Phys. Chem. A*, **102**, 7314–7323.
Bader, R. F. W. (2006). *Chem. Eur. J.* **12**, 2896–2901.
Bader, R. F. W. (2009). *J. Phys. Chem. A*, **113**, 10391–10396.
Bader, R. F. W. & Matta, C. (2004). *J. Phys. Chem. A*, **108**, 8385–8394.
Bader, R. F. W., Slee, T. S., Cremer, D. & Kraka, E. (1983). *J. Am. Chem. Soc.* **105**, 5061–5068.
Bader, R. F. W. & Stephens, M. E. (1975). *J. Am. Chem. Soc.* **97**, 7391–7399.
Balasubramaniyan, V. (1966). *Chem. Rev.* **19**, 691–700.
Becke, A. D. (1988). *Phys. Rev. A*, **38**, 3098–3100.
Becke, A. D. (1993). *J. Chem. Phys.* **98**, 5648–5652.
Biegler-König, F. (2000). *J. Comput. Chem.* **12**, 1040–1048.
Biegler-König, F. W., Bader, R. F. W. & Tang, T.-H. (1982). *J. Comput. Chem.* **3**, 317–328.
Blessing, R. H. (1995). *Acta Cryst.* A**51**, 33–38.
Blessing, R. H. (1997*a*). *DENZOX*. University of Glasgow, Scotland.
Blessing, R. H. (1997*b*). *J. Appl. Cryst.* **30**, 421–426.
Bock, H., Sievert, M. & Havlas, Z. (1998). *Chem. Eur. J.* **4**, 677–685.
Bunge, C. F., Barrientos, J. A. & Bunge, A. V. (1993). *At. Data Nucl. Data Tables*, **53**, 113–162.
Carre, F., Corriu, R. J. P., Kpoton, A., Poirier, M., Royo, G., Young, J. C. & Belin, C. (1994). *J. Organomet. Chem.* **470**, 43–57.
Cheeseman, J. R., Carroll, M. T. & Bader, R. F. W. (1998). *Chem. Phys. Lett.* **143**, 450–548.
Cioslowski, J. & Mixon, S. T. (1992). *J. Am. Chem. Soc.* **114**, 4382–4387.
Cioslowski, J., Mixon, S. T. & Edwards, W. D. (1991). *J. Am. Chem. Soc.* **113**, 1083–1085.
Clark, T., Chandrasekhar, J., Spitznagel, G. W. & Schleyer, P. v. R. (1983). *J. Comput. Chem.* **4**, 294.
Cremer, D., Kraka, E., Slee, T. S., Bader, R. F. W., Lau, C. D. H., Nguyen-Dang, T. T. & MacDougall, P. (1983). *J. Am. Chem. Soc.* **105**, 5069–5075.
Desiraju, G. (1989). *Crystal Engineering: The Design of Organic Solids*. Amsterdam: Elsevier.
Desiraju, G. & Steiner, T. (2001). *The Weak Hydrogen Bond in Structural Chemistry and Biology*. Oxford University Press.
Dominiak, P. M., Petersen, S., Schiemenz, B., Schiemenz, G. P. & Wozniak, K. (2005). *J. Mol. Struct.* **751**, 172–183.
Egli, M., Wallis, J. D. & Dunitz, J. D. (1986). *Helv. Chim. Acta*, **69**, 255–266.
Eichkorn, K., Treutler, O., Öhm, H., Häser, M. & Ahlrichs, R. (1995*a*). *Chem. Phys. Lett.* **240**, 283–289.
Eichkorn, K., Treutler, O., Öhm, H., Häser, M. & Ahlrichs, R. (1995*b*). *Chem. Phys. Lett.* **242**, 652–660.
Eichkorn, K., Weigend, F., Treutler, O. & Ahlrichs, R. (1997). *Theor. Chem. Acc.* **97**, 119–124.
Espinosa, E., Alkorta, I., Elguero, J. & Molins, E. (2002). *J. Chem. Phys. J. Chem. Phys.* **117**, 5529–5542.
Espinosa, E., Alkorta, I., Rozas, I., Elguero, J. & Molins, E. (2001). *Chem. Phys. Lett.* **336**, 457–461.
Espinosa, E., Souhassou, M., Lachekar, H. & Lecomte, C. (1999). *Acta Cryst.* B**55**, 563–572.
Farrugia, L. J. (1997). *J. Appl. Cryst.* **30**, 565.
Farrugia, L. J. (1999). *J. Appl. Cryst.* **32**, 837–838.
Flensburg, C. & Madsen, D. (2000). *Acta Cryst.* A**56**, 24–28.
Frisch, M. J., Pople, J. A. & Binkley, J. S. (1984). *J. Chem. Phys.* **80**, 3265.
Frisch, M. J. *et al.* (2004). *GAUSSIAN*03, Revision E.01. Gaussian Inc., Wallingford, CT.
Gatti, C., May, E., Destro, R. & Cargnoni, F. (2002). *J. Phys. Chem A*, **106**, 2702–2720.
Grimme, S. (2004). *J. Comput. Chem.* **25**, 1463–1473.
Grimme, S. (2006). *J. Comput. Chem.* **27**, 1787–1799.
Grimme, S., Mück-Lichtenfeld, C., Erker, G., Kehr, G., Wang, H., Beckers, H. & Willner, H. (2009). *Angew. Chem. Int. Ed.* **48**, 2592–2595.
Hansen, N. K. & Coppens, P. (1978). *Acta Cryst.* A**34**, 909–921.
Herbstein, F. H. (2000). *Acta Cryst.* B**56**, 547–557.
Hernández-Trujillo, J. & Matta, C. F. (2007). *Struct. Chem.* **18**, 849–857.
Hirshfeld, F. L. (1976). *Acta Cryst.* A**32**, 239–244.
Hirshfeld, F. L. (1977). *Theor. Chim. Acta*, **44**, 129.
Jeffrey, G. A. (1999). *J. Mol. Struct.* **485**, 293–298.
Keith, T. A. (2009). *AIMall*, http://aim.tkgristmill.com.
Keith, T. A., Bader, R. F. W. & Aray, Y. (1996). *Int. J. Quant. Chem.* **57**, 183–198.
Kilian, P., Slawin, A. M. Z. & Woolins, J. D. (2004). *Phosphorus Sulfur Silicon Relat. Elem.* **179**, 999–1002.
Koch, U. & Popelier, P. L. A. (1995). *J. Phys. Chem.* **99**, 9747–9754.
Koritsanszky, T. S. (2006). *Hydrogen Bonding – New Insights*, edited by S. J. Grabowski, pp. 441–470. Dordrecht: Springer.
Koritsanszky, T. S. & Coppens, P. (2001). *Chem. Rev.* **101**, 1583–1627.
Krishnan, R., Binkley, J. S., Seeger, R. & Pople, J. A. (1980). *J. Chem. Phys.* **72**, 650.
Lee, C., Yang, W. & Parr, R. G. (1988). *Phys. Rev. B*, **37**, 785–789.
Lyssenko, K., Aldoshin, S. M. & Antipin, M. Yu. (2004). *Mendeleev Commun.* **14**, 98–100.
Madsen, A. Ø. (2006). *J. Appl. Cryst.* **39**, 757–758.
Madsen, A. Ø., Sørensen, H. O., Flensburg, C., Stewart, R. F. & Larsen, S. (2004). *Acta Cryst.* A**60**, 550–561.
Mallinson, P. R., Smith, G. T., Wilson, C. C., Grech, E. & Wozniak, K. (2003). *J. Am. Chem. Soc.* **125**, 4259–4270.
Mallinson, P. R., Wozniak, K., Wilson, C. C., McCormack, K. L. & Yufit, D. S. (1999). *J. Am. Chem. Soc.* **121**, 4640–4646.
Mata, I., Alkorta, I., Espinosa, E., Molins, E. & Elguero, J. (2007). *The Quantum Theory of Atoms in Molecules – From Solid State to DNA and Drug Design*, edited by C. F. Matta & R. J. Boyd, pp. 425–451. Weinheim: Wiley-VCH.
Matta, C. F. (2006). *Hydrogen Bonding – New Insights*, edited by S. J. Grabowski, pp. 337–375. Dordrecht: Springer.
Matta, C. F., Hernández-Trujillo, J., Tang, T.-H. & Bader, R. F. W. (2003). *Chem. Eur. J.* **9**, 1940–1951.
Meindl, K. & Henn, J. (2008). *Acta Cryst.* A**64**, 404–418.
McKinnon, J. J., Spackman, M. A. & Mitchell, A. S. (2004). *Acta Cryst.* B**60**, 627–668.
McLean, A. D. & Chandler, G. S. (1980). *J. Chem. Phys.* **72**, 650.

Meresse, A., Courseille, C., Leroy, F. & Chanh, N. B. (1975). *Acta Cryst.* B**31**, 1236–1241.
Munshi, P. & Guru Row, T. N. (2005*a*). *Crystallogr. Rev.* **11**, 199–241.
Munshi, P. & Guru Row, T. N. (2005*b*). *CrystEngComm*, **7**, 608–611.
Munshi, P. & Guru Row, T. N. (2005*c*). *J. Phys. Chem. A*, **109**, 659–672.
Munshi, P. & Guru Row, T. N. (2006). *Cryst. Growth Des.* **6**, 708–718.
Munshi, P., Madsen, A. Ø., Spackman, M. A., Larsen, S. & Destro, R. (2008). *Acta Cryst.* A**64**, 465–475.
Nishio, M., Hirota, M. & Umezawa, Y. (1998). *The CH/π interaction: Evidence, Nature and Consequences*. New York: Wiley.
Nonius (1998). *Collect.* Nonius BV, Delft, The Netherlands.
Oddershede, J. & Larsen, S. (2004). *J. Phys. Chem A*, **108**, 1057–1063.
O'Leary, J. & Wallis, J. D. (2006). *Chem. Eur. J.* **12**, 7724–7732.
Omelanczuk, J., Karacar, A., Freytag, M., Jones, P. G., Bartsch, R., Mikolajczyk, M. & Schmutzler, R. (2003). *Inorg. Chim. Acta*, **350**, 583–591.
Otwinowski, Z. & Minor, W. (1997). *Methods in Enzymology*, Vol. 276, *Macromolecular Crystallography*, Part A, edited by C. W. Carter Jr & R. M. Sweet, pp. 307–326. New York: Academic Press.
Pendás, M. A., Francisco, E., Blanco, M. A. & Gatti, C. (2007). *Chem. Eur. J.* **13**, 9362–9371.
Poater, J., Solà, M. & Bickelhaupt, F. M. (2006*a*). *Chem. Eur. J.* **12**, 2889–2895.
Poater, J., Solà, M. & Bickelhaupt, F. M. (2006*b*). *Chem. Eur. J.* **12**, 2902–2905.
Scherer, W., Sirsch, P., Shorokhov, D., McGrady, G. S., Mason, S. A. & Gardiner, M. G. (2002). *Chem. Eur. J.* **8**, 2324–2334.
Scherer, W., Sirsch, P., Shorokhov, D., Tafipolsky, M., McGrady, G. S. & Gullo, E. (2003). *Chem. Eur. J.* **9**, 6057–6070.
Scherer, W., Tafipolsky, M. & Öfele, K. (2008). *Inorg. Chim. Acta*, **361**, 513–520.
Schiemenz, G. P. & Näther, C. (2002). *Z. Naturforsch. B*, **57**, 309–318.
Sheldrick, G. M. (2008). *Acta Cryst.* A**64**, 112–122.
Sierka, M., Hogekamp, A. & Ahlrichs, R. (2003). *J. Chem. Phys.* **118**, 9136–9148.
Spackman, M. A. & Jayatilaka, D. (2009). *CrystEngComm*, **11**, 19–32.
Steiner, T. (1996). *Cryst. Rev.* **6**, 1–57.
Steiner, T. & Desiraju, G. (1998). *J. Chem. Soc. Chem Commun.* pp. 891–892.
Stephens, P. J., Devlin, J. F., Chabalowski, C. F. & Frisch, M. J. (1994). *J. Phys. Chem.* **98**, 11623–11627.
Stone, A. J. (1996). *The Theory of Intermolecular Forces.* Oxford: Clarendon Press.
Su, Z. & Coppens, P. (1998). *Acta Cryst.* A**54**, 646–652.
Tafipolsky, M., Scherer, W., Öfele, K., Artus, G., Pedersen, B., Herrmann, W. A. & McGrady, G. S. (2002). *J. Am. Chem. Soc.* **124**, 5865–5880.
Treutler, O. & Ahlrichs, R. (1995). *J. Chem. Phys.* **102**, 346–354.
TURBOMOLE GmbH (2008). *TURBOMOLE*, Version 5.9.1. TURBOMOLE GmbH, Karlsruhe, Germany.
Volkov, A., Gatti, C., Abramov, Y. & Coppens, P. (2000). *Acta Cryst.* A**56**, 252–258.
Volkov, A., Koritsanszky, T. & Coppens, P. (2004). *Chem. Phys. Lett.* **391**, 170–175.
Volkov, A., Macchi, P., Farrugia, L. J., Gatti, C., Mallinson, P., Richter, T. & Koritsanszky, T. (2006). *XD*2006. University at Buffalo, NY; University of Milano, Italy; University of Glasgow, UK; CNRISTM, Milano, Italy; Middle Tennessee State University, TN, USA.
Vosko, S. H., Wilk, L. & Nusair, M. (1980). *Can. J. Phys.* **58**, 1200–1211.
Vyskočil, S., Meca, L., Tišlerová, I., Císařová, I., Polášek, M., Harutyunyan, S. R., Belokon, Y. N., Stead, R. M. J., Farrugia, L. J., Lockhart, S. C., Mitchell, W. L. & Kočovský, P. (2002). *Chem. Eur. J.* **8**, 4633–4648.
Weigend, F. (2006). *Phys. Chem. Chem. Phys.* **8**, 1057–1065.
Weigend, F. & Ahlrichs, R. (2005). *Phys. Chem. Chem. Phys.* **7**, 3297–3305.
Williams, D. E. & Cox, S. R. (1984). *Acta Cryst.* B**40**, 404–417.
Zarychta, B., Pichon-Pesme, V., Guillot, B., Lecomte, C. & Jelsch, C. (2007). *Acta Cryst.* A**63**, 108–125.
Zhao, Y. & Truhlar, D. G. (2006). *J. Chem. Theory Comput.* **2**, 1009–1018.
Zhao, Y. & Truhlar, D. G. (2008). *Acc. Chem. Res.* **41**, 157–167.
Zhurov, V. V., Zhurova, E. A. & Pinkerton, A. A. (2008). *J. Appl. Cryst.* **41**, 340–349.